Competitive Formation of Ultra-thin Alumina Films at the Fe 0.85 Al 0.15 (110) Surface

Natalia Alyabyeva, Stéphane Chenot, Pascal David, Gregory Cabailh, Jacques Jupille, Alexey Koltsov, Rémi Lazzari

Competitive Formation of Ultra-thin Alumina Films at the $Fe_{0.85}Al_{0.15}$(110) Surface

Natalia Alyabyeva,[†] Stéphane Chenot,[†] Pascal David,[†] Gregory Cabailh,[†] Jacques Jupille,[†] Alexey Koltsov,[‡] and Rémi Lazzari*,[†]

†*CNRS, Sorbonne Université, Institut des NanoSciences de Paris, UMR 7588, 4 Place Jussieu, F-75005 Paris, France*

‡*ArcelorMittal Maizières Research, voie Romaine, F-57280 Maizières-lès-Metz, France*

E-mail: remi.lazzari@insp.jussieu.fr

Abstract

Using surface sensitive techniques (photoemission, low-electron diffraction, scanning tunnelling microscopy), the present work reveals the competitive formation upon oxidation of two epitaxial oxide bilayer films of self-limited thickness on the surface of the ferritic random A2 body-centred alloy $Fe_{0.85}Al_{0.15}$(110). When oxidizing the substrate at 1193 K, a film (herein labelled oxide-A) similar to that studied in depth at NiAl(110) [Kresse *et al.*, Science 308 (2005) 1440] is found. At a slightly lower annealing temperature (1073 K), alumina patches segregated from the bulk act as seeds for the growth of a new long-range ordered alumina film (oxide-B) with two domains having a $\sim (23 \times 23)$ Å^2 hexagonal rotated unit cell. While showing different anion/cation chemical environments, the two films have a $Al_2O_{2.5\pm0.2}$ stoichiometry and stand on an Al-enriched subsurface with a similar ~ 3 nm deep segregation profile. Most importantly, thermal treatments show that the new structure B is more stable than A. This finding conflicts with the apparent ubiquity of oxide-A that has been observed on many substrates of various symmetries and compositions. This competitive formation of ultra-thin alumina oxides questions the origin of their structural (di)similarity and the actual role of these seeds in the structural transition towards thicker alumina films at higher pressure.

1 Introduction

Alumina is a technological relevant oxide with countless applications ranging from abrasive to catalyst support. It appears in a variety of polymorphs (α, γ, κ, δ, θ, etc...) among which some atomic structures are still debated because their meta-stability prevents the synthesis of large single crystals for accurate structural determination.[1–3] For instance, commonly described as a defective spinel,[1–3] the atomic arrangement of γ-Al_2O_3, whose nano-sized powder is often used as a catalyst or as a support, is still controversial. All alumina crystallographic structures are based on a closed-packed oxygen sub-lattice in which the Al cations occupy tetrahedral and/or octahedral sites.[1] Depending on the type of O stacking, several groups can be distinguished: (i) hexagonal closed-packed O sublattice for α and κ structures, (ii) face-centred cubic with occupancy of both types of sites by Al for γ, δ, θ structures, (iii) or more complex stacking (amorphous alumina with Al in tetrahedral sites). The most stable polymorph is the corundum α-Al_2O_3 that is reached via a complex polymorph pathway upon calcination of aluminum hydroxides.[1,2]

To avoid charge effects when studying alu-

mina surfaces by electron probes, in particular scanning tunnelling microscopy, a strong research effort has been devoted to the growth on Al-alloyed single crystal of well-defined oxide films, such as γ-Al_2O_3,[4,5] which could then be used in model catalytic reactions.[2,3] Indeed, low dimensionality can shake up the energetic hierarchy of bulk phases.[6] As in the well-known example of the anatase/rutile forms of TiO_2, γ-Al_2O_3 is more stable than α-Al_2O_3 in the form of nano-sized powder.[7] Common cases are the new structures experimentally observed on NiAl(110)[8–10] and $Ni_3Al(111)$.[11–13] Without bulk counterparts,[14] those oxide films escape the bulk Al_2O_3 stoichiometry. They are made of O-Al-O-Al bilayer sequences with almost coplanar surface anions and cations and unusual Al-distorted hexagon, pentagon and triangle at the interface. The structural puzzle of the $Al_{10}O_{13}$ bilayer studied in depth on NiAl(110)[8–10] is considerably increased by its ubiquity. Alumina films of similar structure are observed on several supports of various symmetries and compositions [NiAl(110),[8,10] $Fe_{0.47}Al_{0.53}(110)$,[15] Cu-9 at.%Al(111),[16] Al/Ni(111)[17] and the complex metallic alloy γ-$Al_4Cu_9(110)$[18]]. We have previously found a similar structure at the (110) surface of $Fe_{0.85}Al_{0.15}$,[19] a ferritic random A_2 body-centred alloy.

Despite the considerable efforts devoted to the structural study of these oxide films, very little has been done to determine their stability. The issue was addressed theoretically by Van Den Bossche *et al.*[20] in the case of nanometer-thick free standing layers. They showed that the stabilization of polymorphs depends on film thickness. The breaking of a few, possibly weak, Al bonds, the refilling of surface cation vacancies and the polarity-induced relaxation are the driving forces which favour one or the other polymorph in the form of a film. The unsupported θ-Al_2O_3 was found to be by far the most stable structure, thus explaining its predominance on transition metal aluminide (100) surfaces [NiAl); CoAl; FeAl] for symmetry and mismatch reasons.[14] However, the role of the substrate is ignored as a relatively poor adhesion energy is assumed.[20] Clearly, theoretical approaches face the difficulty of the simultaneous exploration of the structure and the stability of the complex alumina layers supported on alloys. The issue is of paramount importance since it is of critical interest in bridging the gap between vacuum-prepared layers and alumina encountered in natural or industrial environments. This includes: (i) the difficulty in thickening crystalline thin films of alumina at partial pressures accessible to surface scientific studies[5,21,22] prevents the understanding of the formation of thick alumina at the surfaces of polycrystalline FeAl-alloys[23,24] or NiAl(110)[25] at higher oxygen activities; (ii) the growth of well-structured ultra-thin alumina films as a simple bulk truncation of the most stable polymorphs (e.g. α-Al_2O_3) is not under control; (iii) the understanding of the switch from external to internal oxidation,[26] *i.e.* the transition from surface oxide to precipitates in the bulk as described in the seminal work of Wagner,[27] which would have many potential applications. (An example is given by the $Fe_{0.85}Al_{0.15}$ alloy under study. It serves as a model[19,24,28–30] for steel grades alloyed with light elements such as Al used by industry to lighten cars. The drawback is that the oxygen-induced segregation of those elements forms surface oxides which challenge galvanization of the steel.[31–35] More favourable in terms of adhesion Zn/Fe instead of Zn/oxide interface would be achieved by promoting internal oxidation.)

In such a context, advances in the state of the art can come from appropriate experiments. The motivation of the present work is the observation of two different bilayered aluminum oxide structure on Al-poor random alloy $Fe_{0.85}Al_{0.15}(110)$ as a function of the substrate annealing temperature. The first one (oxide-A) shares all the characteristics (unit cell, composition, thickness, structure, anti-phase domain boundaries, Al 2s and O 1s shifts)[19] of that found on the reference NiAl(110) surface[8,10,14] and many supports. This similarity makes all the more significant the competitive formation of a new structure (oxide-B) which questions the ubiquity and stability of the unique alumina layer which has been identified so far. By

using Scanning tunnelling Microscopy (STM), Low Energy Electron Diffraction (LEED) and X-ray Photoemission Spectroscopy (XPS), the present study explores the topography of pure phases (Section 3.1) and compares the chemical fingerprints, thickness, composition and segregation profile of Al underneath both oxides (Section 3.2). The segregation of oxide seed patches at the origin of the new oxide-B is discussed in Section 3.3 prior to showing the competing formation of the two structures after room-temperature oxidation (Section 3.4). At last, stability diagrams as a function of annealing conditions are established before comparing with the few existing reports of other alumina layers.

2 Methods

Experiments were carried out in an ultra-high vacuum (UHV) vessel including preparation/analysis chambers with base pressures below 1.10^{-10} mbar equipped with several facilities: XPS, LEED and STM. The $Fe_{0.85}Al_{0.15}(110)$ substrate (from Mateck GmbH; diameter 6 mm; thickness 1 mm; miscut below 0.1°) was prepared through repeated cycles of argon sputtering (beam energy 1 keV; total ion current $\sim$ 18 μA) during 30 min at room-temperature followed by annealing at either 1073 K or 1193 K (T_{an1} as noted hereafter) during 15 min. Surface oxidation was performed *in situ* at 1073 K (labelled herein T_{ox}) right after sample annealing without cooling down to lower temperature through exposure to a fixed O_2 dose of 50 L ($\sim$ 5 min at 2.10^{-7} mbar corresponding to 50 Langmuirs; 1 L is defined as $1.33\,10^{-6}$ mbar.s^{-1}). Direct oxidation could be achieved only below 1093 K, meaning that oxygen does not stick at higher temperatures. As a final step, the sample was annealed under UHV during 5-10 min at the same temperature or slightly higher (T_{an2}) by taking into account that the oxide decomposes at 1270 K. A comparison to oxidation at room temperature (RT) followed by progressive annealing was also undertaken to understand the competition between the formation of the two oxide films. All reported temperatures ($\Delta T \simeq 20$ K) were measured on the sample using an infra-red pyrometer with an emissivity fixed at 0.3.[36] Scientific grade ultra-pure Ar and O_2 gases were used.

Surface structures have been analysed by LEED (ErLEED from SPECS) and imaged by STM at RT (RT-STM from ScientaOmicron) in constant current mode using tungsten tips electrochemically etched in KOH and then rinsed in ethanol.[37] STM images were processed using the WSxM software[38] for flattening, line profile and Fourier transform. Aluminum segregation profile, oxide composition and chemistry have been analysed by XPS (see Refs. 19,29 for details) under Al-Kα monochromatic excitation (1486.6 eV; Phoibos 100 hemispherical analyser with delay-line detector from SPECS) at a pass energy of 20 eV for angles ranging from normal ($\Theta = 0°$) to grazing emission ($\Theta = 70°$). The binding energy scale of the analyser has been calibrated on the Fermi edge of coinage clean metals. Traces of carbon-rich stripes at the surface[28] have been found whatever T_{an1} but their presence does not entail the present conclusions as they disappear upon oxidation. The analysed core level (Fe 3p, Al 2p, O 1s) profiles have been accounted using Doniach-Sunjic line shapes[39] with an asymmetry fixed at 0.1 for the metallic components and Voigt profiles with a Lorentzian component fixed at the Al Kα emission width (0.58 eV) for the oxide contributions.[19] Active Shirley background subtraction has been performed during fits.[40] The analyser transmission function and the photoionization cross sections have been accounted for quantitative XPS analysis.

3 Results

3.1 Oxide films: topography and reconstruction

As seen on large scale STM images, drastically different structures are observed upon oxida-

tion at $T_{ox} = 1073$ K depending on whether the $Fe_{0.85}Al_{0.15}(110)$ surface has been prepared by annealing at $T_{an1} = 1193$ K (oxide-A, Figure 1-a,b) or $T_{an1} = 1073$ K (oxide-B, Figure 1-c,d). As the pseudo-hexagonal reconstruction specific of the bare metallic surface[28,30] is absent, oxide films are assumed to cover the whole surface (Figure 1-a,c). Both oxide surfaces exhibit $\sim 30 - 500$ nm wide terraces with 2-40 Å high step bunches that tend to be aligned along the $[1\bar{1}0]_B$ direction for $T_{an1} = 1193$ K. Close-up images reveal $8 - 12$ nm wide striped domains for oxide-A (inset in Figure 1-a).[19] As previously reported,[19] the shift of half of the periodicity between adjacent domains observed when crossing the ~ 3 nm wide defective areas (Figure 1-b), stems from antiphase boundaries allowing the release of the misfit stress between film and substrate.[8,9,19,41–47]

Oxide-B exhibits 200 nm wide ordered domains with faint parallel streaks (inset in Figure 1-c and Figure S1 of Supporting Information (SI)) which, in adjacent domains, are symmetric with respect to the $[1\bar{1}0]_B$ direction as expected for a two-fold substrate symmetry. At larger STM magnification, streaks are seen to result from a well-ordered distorted honeycomb superstructure bounded by defective areas (Figure 1-d) associated to antiphase domain boundaries as in the above case of oxide-A. By tuning the bias voltage on the two different domains of Figure 1-c, a complete contrast reversal is observed between 2.5 V (Figure 2-a,b) and -2.5 V (Figure 2-c,d). Line profiles reveal a large apparent corrugation of $1 - 2$ Å (Figure 2-e). A hexagonal mesh with lattice parameters $a_{ox} \simeq b_{ox} \simeq 23$ Å and rotated by $\alpha_{ox} \simeq 20°$ relative to $[1\bar{1}0]_B$ emerges. The symmetry of domains with respect to $[1\bar{1}0]_B$ is clearly highlighted (Figure 2-f). In this large unit cell (Figure 2-f), images at atomic scale resolution (Figure 3) show an inner hexagonal periodicity of ~ 4.4 Å that matches the unit cell of the corundum (0001) surface (4.76 Å). The oxide-B unit cell corresponds to about (5×5) that network (Figure 3-c).

The radically different LEED patterns from oxide-A (Figure 4-a,b) and B (Figure 4-c,d)

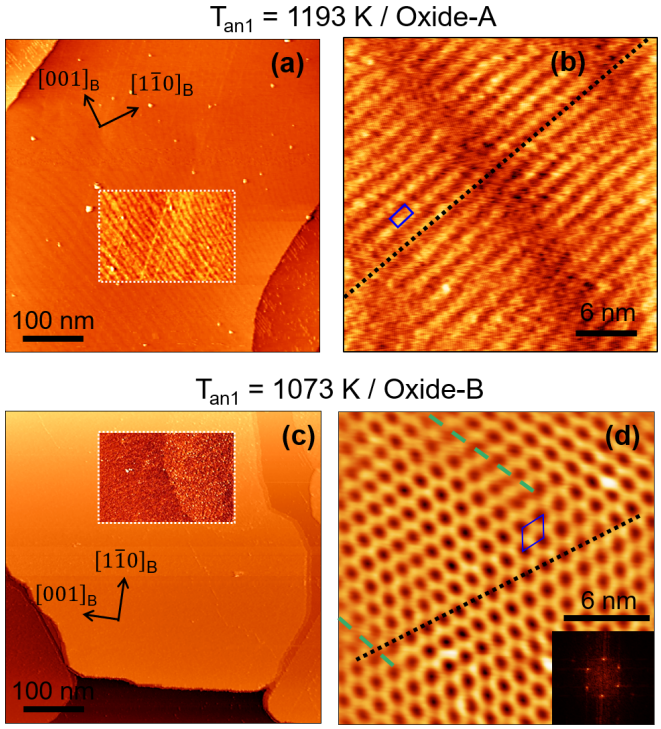

Figure 1: STM (500×500) nm^2 images of alumina films grown by exposure at $T_{ox} = 1073$ K to 50 L of O_2 of $Fe_{0.85}Al_{0.15}(110)$ surfaces pre-annealed at (a)(b) $T_{an1} = 1193$ K (oxide-A; a similar image can be found in Ref. 19) or (c)(d) $T_{an1} = 1073$ K. tunnelling parameters are (a) $U_b = 1$ V, $I_t = 20$ pA; (b) $U_b = -1$ V, $I_t = 12$ pA; (c) $U_b = 2$ V, $I_t = 100$ pA; (d) $U_b = -2.3$ V, $I_t = 20$ pA. Locally enhanced contrasts highlight stripe domains in (a) and a terrace with two domains in (c). Close-up images evidence, in (b), antiphase domain boundaries with a shift of periodicity (black dotted line); in (d), long-range ordered domains (see Fourier transform in inset) bounded by distorted zones (green dotted lines) with a progressive shift of periodicity (dotted black line). The oxide unit cells determined in Ref. 19 or herein are marked in blue in (b) and (d).

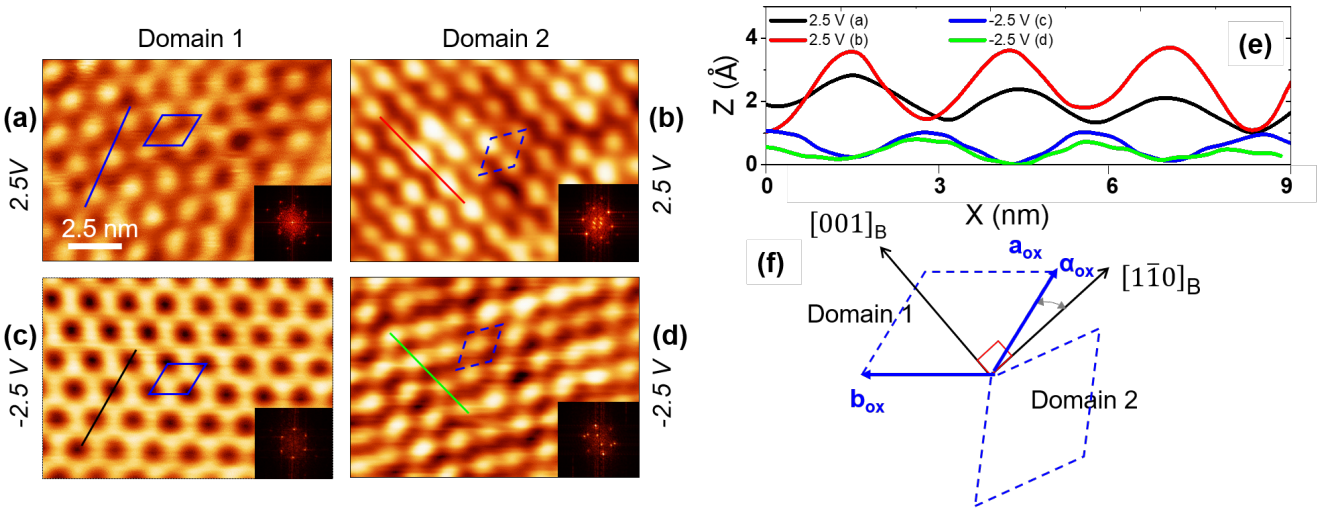

Figure 2: Rotated oxide-B domains shown in Figure 1-d: (a-d) Close-up STM (15×10) nm^2 images with Fourier transform in inset (tunnelling parameters : (a)(b) $U_b = 2.5$ V; (c)(d) $U_b = -2.5$ V with $I_t = 50$ pA); (e) Profiles along the lines shown in figures; (f) Scheme of the unit cells of the two oxide domains (blue dotted parallelograms) compared to substrate unit cell (red rectangle).

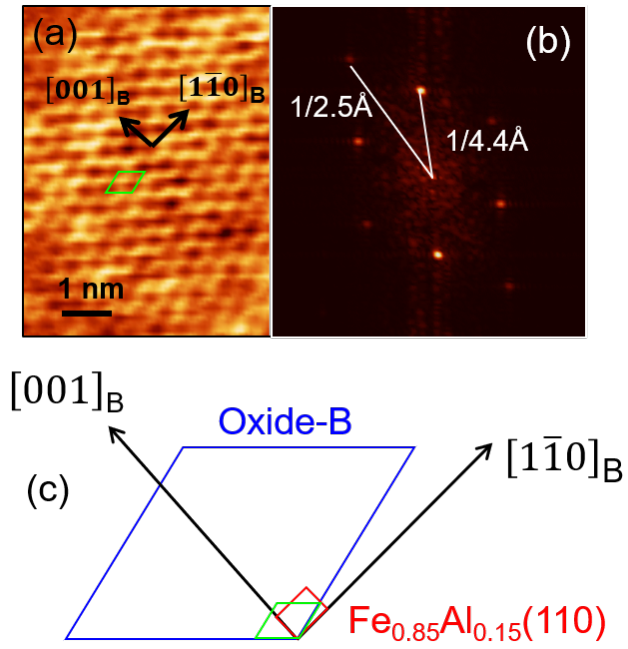

Figure 3: Unit cell of oxide-B: (a) STM at atomic resolution of the alumina film ($U_b = 0.5$ V, $I_t = 12$ pA); (b) Fourier transform that shows a ~ 4.4 Å hexagonal periodicity; (c) oxide, substrate, atomic network unit cells represented by blue, red and green parallelograms, respectively.

surfaces confirm STM findings. Patterns are indexed in the rectangular centred surface unit cell $(\mathbf{a_S}, \mathbf{b_S})$ ($a_s = 4.0891$ Å and $b_s = 2.8914$ Å) aligned along the $[1\bar{1}0]_B$ and $[001]_B$ directions ($a_B = 2.8914$ Å) of the (110) bulk truncation of the A_2 bcc $Fe_{0.85}Al_{0.15}$ alloy.[19,30] The LEED of oxide-A (Figure 4-a,b), similar to that on NiAl(110),[8,10] reveals two mirror domains corresponding to the previously determined[19] (18.8×10.7) Å^2 nearly rectangular unit cell rotated by 27.5° relative to $[1\bar{1}0]_B$. As for oxide-B, a simulation of the $E_K = 65$ eV LEED pattern with two-symmetry related domains based on the unit cell found by STM (see above and Figure 2-f) reproduces qualitatively the main diffraction spots (Figure S2 of SI) and demonstrates that the mesh observed in Figure 1-d and Figure 2 is not simply a Moiré pattern.

3.2 Photoemission from oxide films: chemical environments, subsurface segregation profile, film thickness and stoichiometry

The Al 2p and O 1s core level spectra from oxide films A and B strongly differ despite their

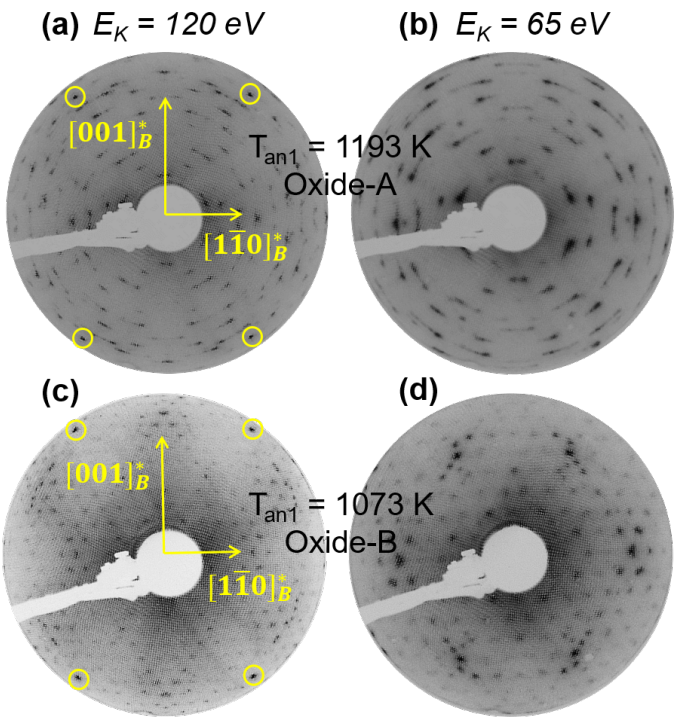

Figure 4: LEED patterns of (a)(b) oxide-A (T_{an1} = 1193 K, T_{ox} = 1073 K) and (c)(d) oxide-B (T_{an1} = T_{ox} = 1073 K) on $Fe_{0.85}Al_{0.15}$(110) at beam energy (a)(c) 120 eV and (b)(d) 65 eV. Due to the centering of the rectangular surface unit cell of the random A_2 alloy, only the substrate reflections circled in yellow are visible. Reciprocal surface directions $[1\bar{1}0]^*_B$ and $[001]^*_B$ are shown with arrows.

similar overall profiles (Figure 5). Both are clearly associated to aluminum oxide since iron is not oxidized at all, as demonstrated by the perfect overlap of the Fe 3p spectra from bare and oxidized surfaces even for surface sensitive analysis (Figure 6-a and Ref. 19). The Al 2p profile of the two oxide films could be decomposed into three components,[19] each including two spin-orbit split levels (Figure 6 for oxide-B and Ref. 19 for oxide-A). Common to all preparations, the binding energy E_B = 72.1 eV of the metallic component is characteristic of aluminide compounds.[19,48] The two others are assigned to interface and surface oxidized Al through their relative change in intensity with emission angle. O 1s spectra have two components of which the higher energy ones are associated with surface O atoms of the oxides. Parameters derived from fits are gathered in Tables S1 (Al 2p) and S2 (O 1s) of SI. Sizeable differences are observed between the two oxides films. Compared to the reported fit of the photoemission data of oxide-A,[19] a shift of $\sim$ 0.4 eV, an increase of $\sim$ 20 % in intensity and a broadening of $\sim$ 0.4 eV are observed for the Al 2p core level of the oxide-B. Similar changes are observed for the O 1s surface component.

The Al segregation profile and the subsurface composition have been examined through the angular dependence of core level area ratios. On all surfaces, either bare or oxidized, whatever the annealing temperature, the Al segregation profile determined via the $I_{Al\ 2p(met)}/I_{Fe\ 3p(met)}$ ratio[19] is the same within error bars (Figure S3 of SI). Over a depth of 30$-$40 Å, the subsurface average composition is close to $Fe_{0.6}Al_{0.4}$ which corresponds on average to a CsCl B_2 structure on the basis of the bulk phase diagrams.[49,50] These findings are in line with the bulk Al mobility above 700 K and the stationary segregation profile above 1000 K which were already observed on the bare substrate.[29] In the same way as for oxide-A,[19] the thickness and stoichiometry of oxide-B have been derived from the angular analysis of $I_{Al\ 2p(ox)}/I_{Fe\ 3p(met)}$, $I_{O\ 1s(ox)}/I_{Fe\ 3p(met)}$, $I_{Al\ 2p(ox)}/I_{Al\ 2p(met)}$ and $I_{O\ 1s(ox)}/I_{Al\ 2p(met)}$ (Figure S3-S4 of SI and Ref. 19). The B-film was found under-stoichiometric

in oxygen compared to bulk alumina (Al_2O_3) with a similar average composition ($Al_2O_{2.5\pm0.2}$) and thickness (~ 6 Å) as oxide-A.

The difference in structure and chemistry of the two oxide bilayers apparently relies on the annealing temperature of the bare substrate prior to oxidation. This point is now examined.

3.3 Oxide patches after annealing the $Fe_{0.85}Al_{0.15}$(110) surface at low temperature

The Al 2p and O 1s spectra show traces of surface oxidation after annealing at $T_{an1} = 1073$ K (Figure 5 and Figure 6-b,c). In contrast, the preparation at $T_{an1} = 1193$ K leads to a perfect metallic surface.[19] Repeated cycles of sample preparation gave the same photoemission profiles. It is now shown that these traces of oxide play a central role in the formation of oxide-B.

During progressive annealing from RT to $T_{an1} = 1123$ K right after sample sputtering, the O 1s intensity increases steadily until reaching a maximum at $\sim$ 800 K as the segregation of Al begins[29] (Figure 7-a,b). At 1223 K, the surface oxide completely disappears, by either desorption or dissolution in the bulk. The localization of the oxidized areas after $T_{an1} = 1073$ K was explored via angular measurements of $I_{O\ 1s}/I_{Fe\ 3p(met)}$ and $I_{O\ 1s}/I_{Al\ 2p(met)}$. To remove the variation in intensity due to the damping of Al and Fe signals in the substrate signal, data have been normalized by the previously obtained intensity profile of metallic Fe 3p and Al 2p after Al-segregation[19,29] (see Section 3.2 and Figure S3 of SI). O 1s areas determined experimentally clearly escape the $\cos\Theta$ profile expected for a homogeneous bulk distribution of oxygen (Figure 7-c). They rather correspond to oxidized species at the surface, the signal of which is poorly damped. Quantification with a model of continuous bulk Al_2O_3 film gives an average submonolayer thickness of ~ 0.5 Å.

After $T_{an1} = 1073$ K, the LEED pattern at a beam energy of $E_K = 120$ eV (Figure 8-a) is similar to that obtained at $T_{an1} = 1193$ K[30] with "flower"-like spots around the (1×1) active reflections assigned to the incommensurate pseudo-hexagonal 18 Å-large Al-rich surface reconstruction of the bare surface[30] (see Figure 9-c). However, additional low-intensity LEED spots are observed at $E_K = 65$ eV (Figure 8-b) that are not seen after annealing at $T_{an1} = 1193$ K (Figure 8-c). They show an overall hexagonal periodicity that matches that of the fully formed oxide-B layer (Figure 4-d). In parallel, on the two oxide surfaces, STM reveals terraces separated by multiatomic steps with much different shapes and orientations (inset in Figure 9-a,b). $T_{an1} = 1193$ K leads to rather straight steps preferentially aligned along $[1\bar{1}0]_B$ (Figure 9-a) (see also Refs. 28,30) while, for $T_{an1} = 1073$ K, they are more rounded and delimit irregular zones with a different contrast, called hereafter patches (Figure 9-b). Close-up images recorded on the terraces of both surfaces (Figure 9-c,d) evidence the pseudo-hexagonal 18 Å unit cells, also corresponding to the "flower-like" LEED patterns (Figure 8-a), which characterize the bare metal surface.[30] At the opposite, patches show drastically different bias-dependent STM contrasts (Figure 9-d and 10). The locally ordered honeycomb structures that appear at ± 2.5 V with a $\sim$ 2 nm periodicity closely resemble those recorded upon STM analysis of the oxide-B (Figure 1-d and Figure 2). Those converging evidences demonstrate that patches corresponds to oxidized area already identified by LEED. Patches occupy around 30 % of the surface but their coverage does not increase with the annealing time (from 5 to 60 min), as seen by STM (Figure S5 of SI) and XPS (not shown). In line with Figure 7-a, the observation rules out any role of the residual gases during annealing in the patches formation but instead favours a self-limited segregation from the bulk. Combined with the average thickness of ~ 0.5 Å obtained from photoemission, this coverage gives patches with a height of a monolayer (~ 1.7 Å), which explains a different STM appearance compared to the full layer (Figure 10 vs Figure 2).

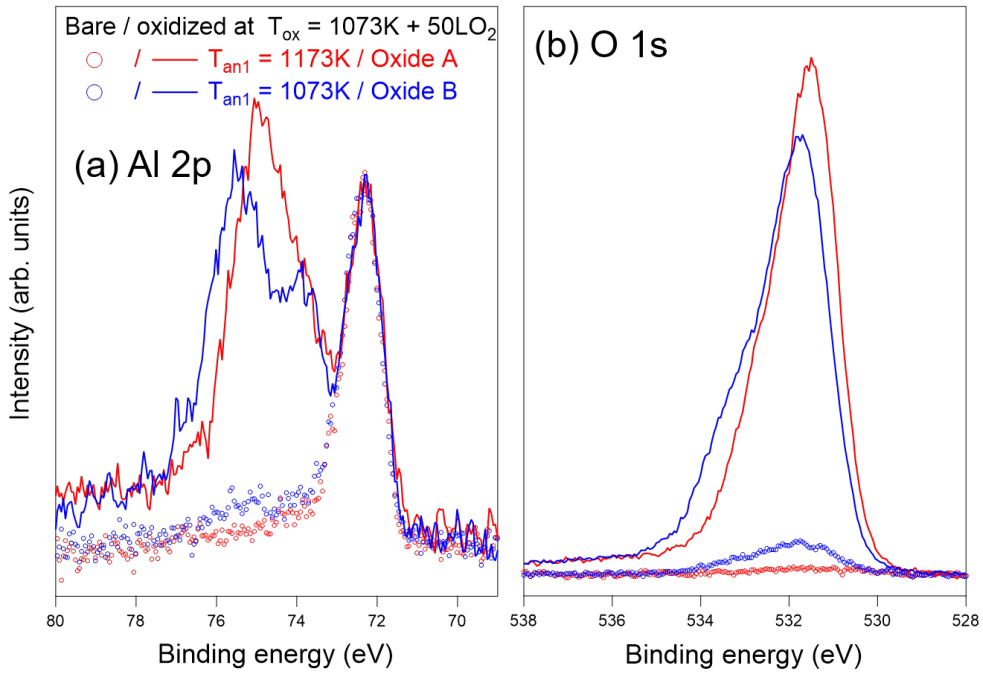

Figure 5: Comparison of XPS core levels of the bare $Fe_{0.85}Al_{0.15}(110)$ surface to those of the surfaces oxidized at $T_{ox} = 1073$ K after annealing at either $T_{an1} = 1193$ K (oxide-A) or $T_{an1} = 1073$ K (oxide-B): (a) Al 2p; (b) O 1s.

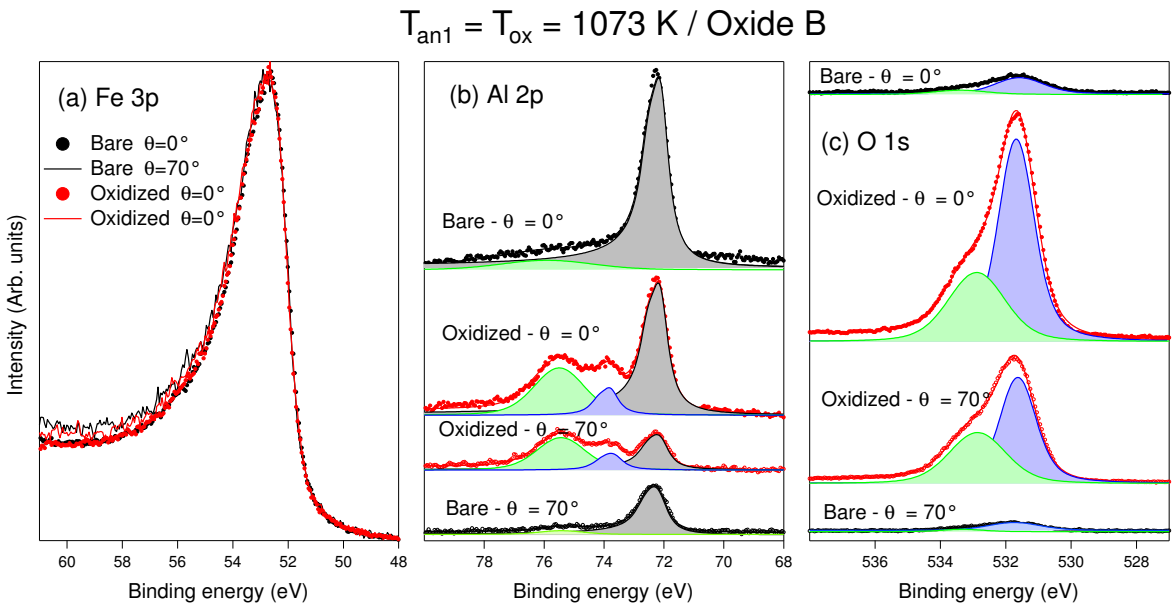

Figure 6: Photoemission from oxide-B surfaces: (a) Fe 3p; (b) Al 2p; (c) O 1s. Spectra of the clean ($T_{an1} = 1073$ K in vacuum) and oxidized (50 L of O_2 at 1073 K) surfaces are compared at normal ($\Theta = 0°$) and grazing ($\Theta = 70°$) emissions. For Al 2p spectra, three doublets are needed to fit (lines) the data (points) recorded on oxide layers; each corresponds to the superposition of the 2p 1/2 and 2p 3/2 levels with a 0.4 eV spin-orbit split.[51] For O 1s spectra, only two components are required. Voigt and Doniach-Sunjic profiles are used to account for oxide and metal components, respectively. A similar decomposition can be found in Ref. 19 for oxide-A.

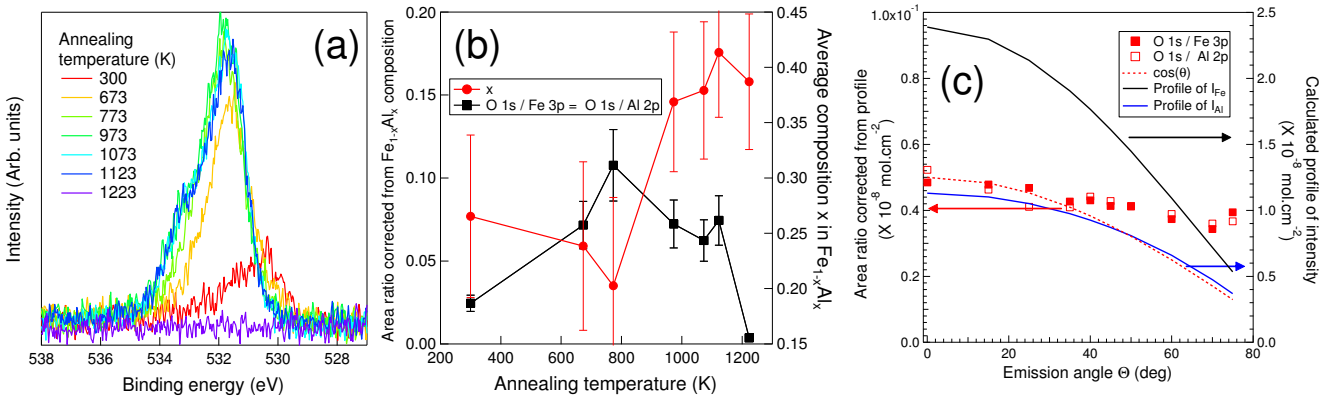

Figure 7: Photoemission analysis of residual oxide patches upon annealing of a sputtered surface: (a) O 1s core level. The slight contamination of the highly reactive surface sputtered at RT gives rise to a specific chemical shift (see below Section 3.4). Oxygen segregates at increasing annealing temperature with a maximum at T_{an1} = 773 K followed by a decrease. An O-free but Al-rich surface is routinely obtained after T_{an1} = 1193 K[19] which discards any sizeable effect of vacuum contamination; (b) (left scale) O 1s/Al 2p(met) and O 1s/Fe 3p(met) ratios of core level areas after correction from a fictitious composition $Fe_{1-x}Al_x$ as deduced from metallic Al 2p/Fe 3p ratio (right scale); (c) angular dependence of $I_{O\ 1s}/I_{Al\ 2p}$ and $I_{O\ 1s}/I_{Fe\ 3p}$ (symbols) corrected from the determined profile of Al/Fe composition (black/blue lines); a comparison is made with the $\cos\Theta$ trend expected for a species dissolved in the bulk.

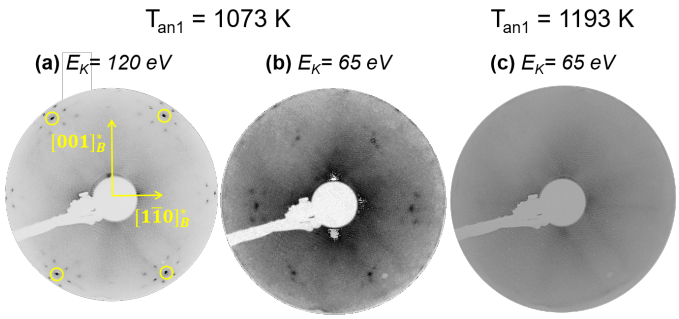

Figure 8: LEED patterns of the $Fe_{0.85}Al_{0.15}(110)$ surface for beam kinetic energies and annealing temperatures of (a) 120 eV, T_{an1} = 1073 K; (b) 65 eV, T_{an1} = 1073 K; (c) 65 eV, T_{an1} = 1193 K. The active spots of the substrate circled in yellow (Figure a) are surrounded by those of the bare metal reconstruction. Weak spots related to oxide patches show up at 65 eV in (b) for T_{an1} = 1073 K (Figure b) but are absent in (c) after T_{an1} = 1193 K.

The assignment to oxide patches of the LEED spots recorded after annealing at T_{an1} = 1073 K in vacuum (Figure 8-b) is confirmed as they get more intense and sharpen after an O_2 dose (10 L) at $T_{an1} = T_{ox}$ = 1073 K (Figure S6-a,b of SI). This evolution parallels a slight increase in coverage to $\sim$ 40 % and mainly a thickening of patches up to the final value of $\sim$ 7.5 Å (XPS mean thickness of $\sim$ 3 Å) (Figure S6-c of SI). Large dose up to 500 L (Figure S7 of SI) leads to the formation of a full oxide-B layer (Section 3.1). But no further thickening of the film could be observed by photoemission for the explored exposures.

Therefore, oxidized surface patches formed after annealing the bare surface at T_{an1} = 1073 K or below act as seeds for the growth of oxide-B while a direct oxidation of a patch-free surface obtained at T_{an1} = 1193 K leads to oxide-A. Patches of oxide-B segregate at mild temperature but disappear upon further annealing. This raises the question of the relative stability of the two oxides as a function of the temperature of formation. To try to solve it, the

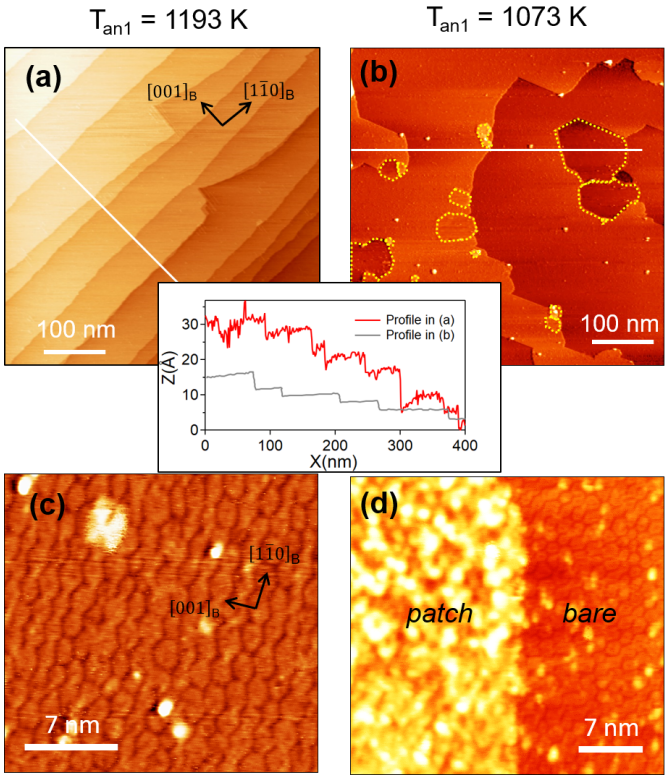

Figure 9: STM analysis of $Fe_{0.85}Al_{0.15}(110)$ surfaces after annealing in vacuum: (a)(b) (500 × 500) nm^2 images after (a) T_{an1} = 1193 K (U_b = 2 V, I_t = 150 pA) (see also Ref. 30) and (b) T_{an1} = 1073 K (U_b = 1 V, I_t = 100 pA). Patches are delimited by yellow dotted lines; (c) Close-up STM images of surface reconstruction at U_b = 2.5 V (I_t = 15 − 50 pA) (see also Ref. 30); (d) the frontier between a patch and the bare surface.

annealing of surfaces exposed to oxygen at RT has been explored.

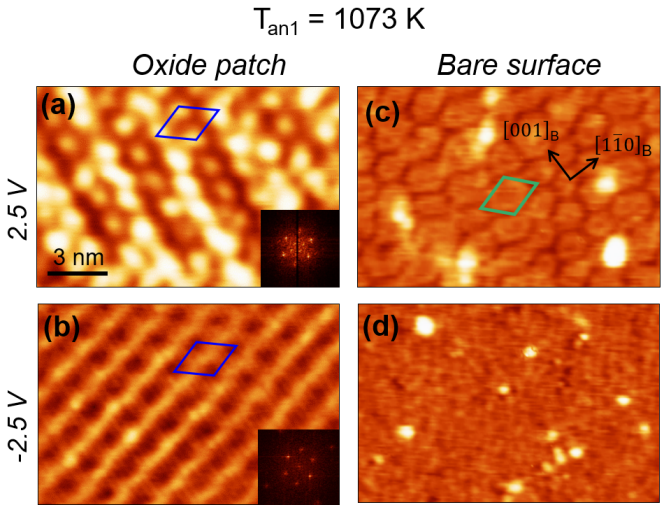

Figure 10: (15 × 15) nm^2 STM images of $Fe_{0.85}Al_{0.15}(110)$ surface annealed at T_{an1} = 1073 K: (a)(b) surface structure of patches with Fourier transforms in inset; (c)(d) bare surface. The rhombs evidence the unit cells of the oxide (in blue) and of the bare surface (in green). STM parameters: (a) U_b = 2.5 V, I_t = 50 pA; (b) U_b = −2.5 V, I_t = 50 pA; (c) U_b = 2.5 V, I_t = 50 pA; (d) U_b = −2.5 V, I_t = 12 pA.

3.4 Competition between oxides: annealing after room-temperature oxidation

Oxidation was performed with a fixed O_2 dose of 50 L at RT followed by further annealing (T_{an2}). Whatever T_{an1}, the exposure lifts the metallic surface reconstruction and leads to an amorphous oxide (Figure S8 of SI). However, for a surface annealed at T_{an1} = 1073 K, a faint LEED pattern characteristic of the oxide patches is still present (Figure S8 of SI). The subsequent recrystallization annealing at T_{an2}=973-1123 K leads to a superposition of the LEED patterns of the two oxides (Figure 11-a,b and Figure S8 of SI) as formed by direct oxidation at T_{ox} = 1073 K (Figure 4). After T_{an2} = 1073 K, STM evidences domains of 10-120 nm in size (Figure 11-c,d). Some of them

show the bias-dependent structure characteristic of oxide-B. The other exhibit stripes indicative of the antiphase domain boundaries of the oxide-A[19] (Figure 1-a,b). All structures have a $\sim$ 2 nm periodicity as confirmed by the analysis in Fourier space (insets of Figure 11-e,f). A further annealing to T_{an2} = 1223 K leads to a surface reorganization into only the oxide-B structure (Figure S8 of SI), as observed at T_{an1} = 1073 K/T_{ox} = 1073 K (Figure 4-c,d). Finally, the oxide LEED pattern disappears at T_{an2} = 1273 K and reverts to that of the bare O-free $Fe_{0.85}Al_{0.15}$(110) surface (Figure S8 of SI). For an initially O-free surface (T_{an1} = 1193 K), a mix of LEED patterns of the two structures is observed for 300 < T_{an2} < 1073 K (Figure S8 of SI). Then, upon annealing at $T_{an2} \simeq 1073 - 1223$ K the oxide-B dominates. It worth reminding that this effect of post-oxidation annealing T_{an2} is effective only after O_2 exposure at RT. Indeed, the structure obtained directly at T_{ox} = 1073 K, whatever its nature, is stable up to its decomposition at 1273 K.

The picture regarding the enhanced stability of oxide-B is confirmed by photoemission. Whatever the initial surface, spectra after RT oxidation are characteristic of an amorphous oxide with a partially dissociated O_2 molecule (Figure S9 of SI). At intermediate T_{an2} temperatures (not shown), the spectroscopic fingerprints of the two oxides overlap. But, for annealing just under the oxide decomposition temperature (T_{an2} = 1223 K), whatever T_{an1}, XPS spectra are characteristic of oxide-B (Figure S10 of SI).

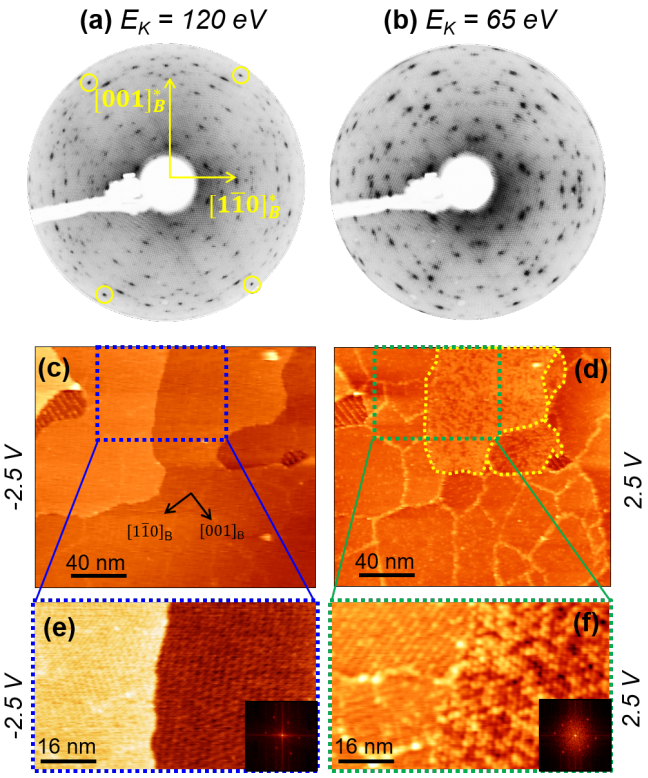

Figure 11: $Fe_{0.85}Al_{0.15}$(110) surface annealed at T_{an1} = 1073 K, exposed to 50 L of O_2 at T_{ox} = 300 K and subsequently annealed at T_{an2} = 1073 K: LEED patterns at a beam energy of (a) 120 eV and (b) 65 eV; (200×200) nm^2 STM images: (c)(e) $U_b = -2.3$ V, I_t = 12 pA; (d)(f) U_b = 2.3 − 2.5 V, I_t = 12 pA. Images (e)(f) with their Fourier transform in inset are close-ups of (c)(d), as indicated by dashed frames.

4 Discussion

While pure oxide-A and B films can be obtained by direct high temperature oxidation, starting from either clean or patch-covered surface, respectively, the progressive annealing after RT oxidation leads to a mixed phase but always ends up with the long-range ordered oxide-B. This competitive formation of oxide films points to their structural (di)similarity. Within the accuracy of photoemission, the two films have the same average composition $Al_2O_{2.5\pm0.2}$,

a thickness close to a bilayer (Figure S4 of SI). They grow on a Al-enriched subsurface with a composition close to FeAl (Figure S3 of SI) similar to that of the bare surface. They involve surface and interfacial Al and O atoms with specific chemical environments as testified by the values of the chemical shifts (Figure 5). Finally, they show similar antiphase domain boundaries oriented perpendicularly to one axis of the substrate unit cell (Figure 1) which are suggested to release the strain due to the misfit with the substrate.[8,9,41–47] Nevertheless, their structures composed of two symmetry-related domains truly differ (Figure 1-4). The oxide of type A obtained by oxidation of an O-free substrate seems to be ubiquitous as it was grown on various supports of different symmetries: NiAl(110),[8,10] $Fe_{0.47}Al_{0.53}$(110),[15,19] Cu-9 at.%Al(111),[16] Al/Ni(111)[17] and the complex metallic alloy γ-Al_4Cu_9(110).[18] At the opposite, there is to our knowledge only one STM report of a bilayer oxide film with a similar rotated hexagonal unit cell of 19 Å; observed at the FeAl(110) surface,[52,53] its reported characteristics seem however different from oxide-B. Using a multi-step oxidation/annealing preparation, Krukowski *et al.*[21] found also on NiAl(110) a common hexagonal atomic arrangement with a periodicity of 2.7 Å superimposed on 45 Å honeycomb periodic modulation. Based on the similarity to oxygen-oxygen interatomic distance, they assigned it to the formation of an α-Al_2O_3 layer, which bears some similarity with the present oxide-B (Figure 3). Unfortunately, in the two cases, there exists no LEED which could be compared to the present findings. In the absence of a deeper crystallographic analysis input, no definitive conclusions regarding the structure of oxide-B and its (di)similarity with known alumina polymorphs can be drawn based on the present measurements (Figure 3). Nevertheless, the hexagonal symmetry and the closeness of unit cells (Figure 3) favours a bilayer of corundum structure although the bulk stoichiometry is not fulfilled.

Effects of the pre-oxidation (T_{an1}) and post-oxidation (T_{an2}) substrate annealing temperatures are summarized in the stability diagrams shown in Figure 12. Starting from an O-free surface[19] ($T_{an1} > 1123$ K), the oxidation lifts rapidly the Al-rich hexagonal reconstruction of the bare surface to form covering oxide-A (Figure 12-a). At the opposite, for $300 < T_{an1} < 1073$ K after sputtering, the Al-rich surface reconstruction[28,30] coexists with oxide patches (phase Φ_{seed}). Monolayer-high patches appear preferentially at step edges (Figure S2 of SI) and act as seeds for the formation of a long range ordered oxide B (Φ_{OxB}) upon oxidation at 1073 K (Figure 12-a). As the oxidation via residual vacuum can be ruled out, oxide patches are assumed to form via segregation from the bulk in parallel to Al mobility as described earlier.[29] This questions the origin of the internal oxides or dissolved oxygen that escape photoemission analysis and their role in the formation of thicker γ-alumina films at higher pressures.[23,24] These points are intimately related to the interplay between external and internal oxidation as studied in depth in corrosion science[24,26] and initially formalised in the Wagner theory of alloy oxidation.[27]

The diagram is more complex for room temperature oxidation (Figure 12-b). The formed amorphous oxide (Φ_{amor}) coexists (or not) with B-type oxide patches depending on the initial substrate annealing temperature. It requires a subsequent annealing at least at $T_{an2} = 773$ K to recrystallize, first in a mixed Φ_{OxA}/Φ_{OxB} phase ($973 \leq T_{an2} \leq 1123$ K) and then in a pure B-type oxide, which, in this process, appears more stable than oxide-A. Finally, both types of alumina layers decompose totally above $T_{an2} \geq 1273$ K either by desorption or redissolution in the bulk.

To pinpoint the transition towards thicker γ-Al_2O_3 films and internal oxidation,[23–25] the extension of such stability diagram at higher oxygen pressures is currently explored using a dedicated annealing cell connected to the vacuum chamber.

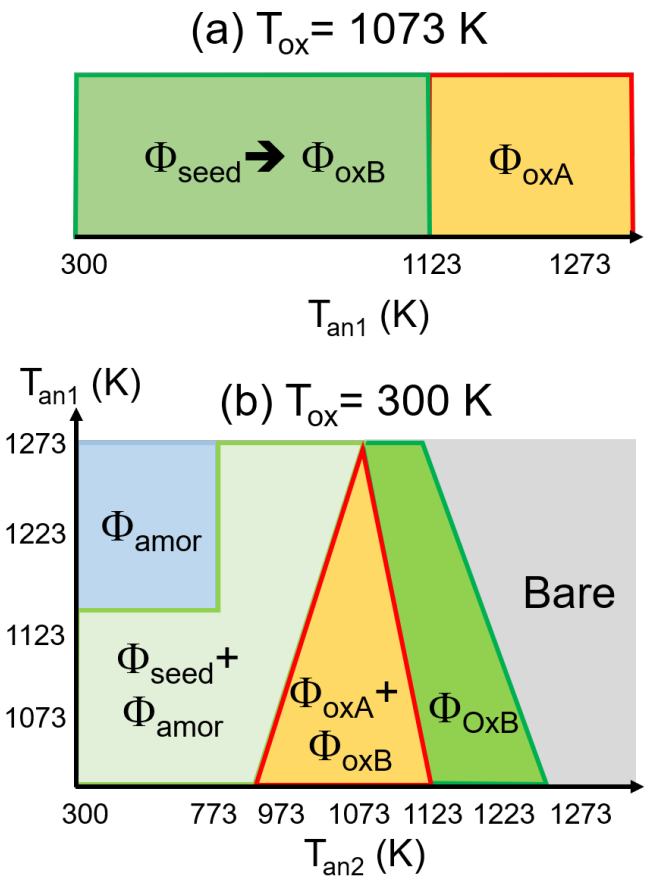

Figure 12: Schematic stability diagram summarizing observations for $Fe_{0.85}Al_{0.15}(110)$ oxidation at (a) $T_{ox} = 1073$ K and (b) $T_{ox} = 300$ K after a substrate annealing at T_{an1} prior to oxidation or after a post-oxidation annealing at T_{an2} : (i) Φ_{OxA}/Φ_{OxB} correspond to the fully covering oxides, (ii) Φ_{seed} to a reconstructed metallic surface covered by B-type oxide patches, (ii) Φ_{amor} to the amorphous oxide.

5 Conclusion

The formation by selective oxidation of alumina films at the surface (110) of the random alloy $Fe_{0.85}Al_{0.15}$ has been explored as a function of the substrate preparation. Two well-crystallized bilayers of oxides are competitively formed. They sit on a Al-enriched FeAl subsurface and have similar sub-stoichiometric composition ($Al_2O_{2.5}$), but their atomic structures and their cation/anion chemical environments strongly differ. The oxide-A formed by direct oxidation of a clean surface annealed at 1193 K corresponds to the well-known oxide film observed on NiAl(110) with a rectangular (18.8×10.7) Å^2. The oxide-B presents a large scale hexagonal unit cell of ~ 23 Å rotated by $\sim 20°$ from $[1\bar{1}0]_B$ direction. Oxide-B grows from pre-existing seeds that segregate from the bulk upon annealing in parallel to Al and cover about 30 % of the surface. Most importantly, annealing treatments show that oxide-B is more stable than oxide-A. The presence of oxidized species in the bulk, *i.e* internal oxide or dissolved oxygen, and their segregation at the surface ask for their actual role in the observed thickening of alumina films at higher pressures.

Acknowledgement The present work benefited from the support of Agence Nationale de la Recherche–France in the frame of project SURFOX (Project No. ANR-16-CE08-0034-01).

Supporting Information Available

Complementary figures of STM, LEED and XPS.

References

(1) Levin, I.; Brandon, D. Metastable alumina polymorphs: crystal structures and transition sequences. *J. Am. Ceram. Soc.* **1998**, *81*, 1995–2012.

(2) Busca, G. The surface of transitional alu-

minas: a critical review. *Catal. Today* **2014**, *226*, 2–13.

(3) Bara, C.; Devers, E.; Digne, M.; Lamic-Humblot, A. F.; Pirngruber, G. D.; Carrier, X. Surface science approaches for the preparation of alumina-supported hydrotreating catalysts. *ChemCatChem* **2015**, *7*, 3422–3440.

(4) Jensen, T. N.; Meinander, K.; Helveg, S.; Foster, A. S.; Kulju, S.; Musso, T.; Lauritsen, J. V. Atomic structure of a spinel-like transition $Al_2O_3(100)$ surface. *Phys. Rev. Lett.* **2014**, *113*, 106103.

(5) Zabka, W.-D.; Leuenberger, D.; Mette, G.; Osterwalder, J. From two- to three-dimensional alumina: interface templated films and formation of $\gamma - Al_2O_3(111)$ nuclei. *Phys. Rev. B* **2017**, *96*, 155420.

(6) Peintinger, M. F.; Kratz, M. J.; Bredow, T. Quantum-chemical study of stable, meta-stable and high-pressure alumina polymorphs and aluminum hydroxides. *J. Mater. Chem. A* **2014**, *2*, 13143–13158.

(7) McHale, J. M.; Auroux, A.; Perotta, A. J.; Navrotsky, A. Surface energies and thermodynamic phase stability in nanocrystalline aluminas. *Science* **1997**, *277*, 788–791.

(8) Libuda, J.; Winkelmann, F.; Baumer, M.; Freund, H. J.; Bertrams, T.; Neddermeyer, H.; Mailer, K. Structure and defects of an ordered alumina film on NiAl(110). *Surf. Sci.* **1994**, *318*, 61.

(9) Stierle, A.; Renner, F.; Streitel, R.; Dosch, H.; Drube, W.; Cowie, B. X-ray diffraction study of the ultrathin Al_2O_3 layer on NiAl(110). *Science* **2004**, *303*, 1652–1656.

(10) Kresse, G.; Schmid, M.; Napetschnig, E.; Shishkin, M.; Köhler, L.; Varga, P. Structure of the ultrathin aluminum oxide film on NiAl(110). *Science* **2005**, *308*, 1440.

(11) Degen, S.; Krupski, A.; Kralj, M.; Langner, A.; Becker, C.; Sokolowski, M.; Wandelt, K. Determination of the coincidence lattice of an ultra thin Al_2O_3 film on Ni_3Al (111). *Surf. Sci.* **2005**, *576*, L57–L64.

(12) Schmid, M.; Kresse, G.; Buchsbaum, A.; Napetschnig, E.; Gritschneder, S.; Reichling, M.; Varga, P. Nanotemplate with holes: ultrathin alumina on $Ni_3Al(111)$. *Phys. Rev. Lett.* **2007**, *99*, 196104.

(13) Vesselli, E.; Baraldi, S., A. Lizzit; Comelli, G. Large interlayer relaxation at a metal-oxide interface: the case of a supported ultrathin alumina film. *Phys. Rev. Lett.* **2010**, *105*, 046102.

(14) Wu, Q.; Fortunelli, A.; Granozzi, G. Preparation, characterisation and structure of Ti and Al ultrathin oxide films on metals. *Int. Rev. Phys. Chem.* **2009**, *28*, 517–576.

(15) Graupner, H.; Hammer, L.; Heinz, K.; Zehner, D. Oxidation of low-index FeAl surfaces. *Surf. Sci.* **1997**, *380*, 335.

(16) Napetschnig, E.; Schmid, M.; Varga, P. Ultrathin alumina film on Cu-9at% Al (111). *Surf. Sci.* **2008**, *602*, 1750–1756.

(17) Prévot, G.; Le Moal, S.; Bernard, R.; Croset, B.; Lazzari, R.; Schmaus, D. Archetypal structure of ultrathin alumina films: Grazing-incidence x-ray diffraction on Ni(111). *Phys. Rev. B* **2012**, *85*, 205450.

(18) Wardé, M.; Ledieu, J.; Serkovic Loli, L.; Herinx, M.; de Weerd, M.-C.; Fournée, V.; Le Moal, S.; Barthés-Labrousse, M.-G. Growth and structure of ultrathin alumina films on the (110) surface of γ-Al_4Cu_9 complex metallic alloy. *J. Phys.: Condens. Matter* **2014**, *26*, 485009.

(19) Dai, Z.; Alyabyeva, N.; Van den Bossche, M.; Borghetti, P.; Chenot, S.; David, P.; Koltsov, A.; Renaud, G.; Jupille, J.; Cabailh, G. et al. Oxide at

the Al-rich $Fe_{0.85}Al_{0.15}(110)$ surface. *Phys. Rev. Materials* **2020**, *4*, 074409.

(20) Van den Bossche, M.; Noguera, C.; Goniakowski, J. Understanding the structural diversity of freestanding Al_2O_3 ultrathin films through a DFTB-aided genetic algorithm. *Nanoscale* **2020**, *12*, 6153–6163.

(21) Krukowski, P.; Chaunchaiyakul, S.; Minagawa, Y.; Yajima, N.; Akai-Kasaya, M.; Saito, A.; Kuwahara, Y. Anomalous hexagonal superstructure of aluminum oxide layer grown on NiAl (110) surface. *Nanotechnology* **2016**, *27*, 455708.

(22) Meyer, T.; Nilius, N. Tungsten deposits facilitate oxidation of the NiAl(110) surface. *The Journal Chemical Physics* **2019**, *150*, 124701.

(23) Cavallotti, R. Effets de la terminaison de l'α-alumine sur le comportement au mouillage du zinc. Ph.D. thesis, Pierre and Marie Curie University, France, 2014.

(24) Drouet, G. Selective oxidation of FeAl alloys. Ph.D. thesis, University Paris-Saclay, 2021.

(25) Vlad, A.; Stierle, A.; Kasper, N.; Dosch, H.; Rühle, M. In situ X-ray study of the γ to α-Al_2O_3 phase transformation during atmospheric pressure oxidation of NiAl(110). *J. Mater. Res.* **2006**, *21*, 3047–3057.

(26) Young, D. Y. *High Temperature Oxidation and Corrosion of Metals (Second Edition)*; Elsevier, 2016.

(27) Wagner, C. Reaktionstypen bei der Oxydation von Legierungen. *Zeitschrift f"ur Elektrochemie, Berichte der Bunsengesellschaft für physikalische Chemie* **1959**, *63*, 772–782.

(28) Dai, Z.; Borghetti, P.; Mouchaal, Y.; Chenot, S.; David, P.; Jupille, J.; Cabailh, G.; Lazzari, R. Self-organized carbon-rich stripe formation from competitive carbon and aluminium segregation at $Fe_{0.85}Al_{0.15}(110)$ surfaces. *Appl. Surf. Sci.* **2018**, *444*, 457–466.

(29) Dai, Z.; Borghetti, P.; Chenot, S.; David, P.; Jupille, J.; Cabailh, G.; Goniakowski, J.; Lazzari, R. Aluminium segregation profiles in the (110), (100) and (111) surface regions of the $Fe_{0.85}Al_{0.15}$ random body-centered cubic alloy. *Appl. Surf. Sci.* **2019**, *492*, 886–895.

(30) Dai, Z.; Alyabyeva, N.; Borghetti, P.; Chenot, S.; David, P.; Koltsov, A.; Renaud, G.; Jupille, J.; Cabailh, G.; Lazzari, R. Al-rich $Fe_{0.85}Al_{0.15}(100)$, (110) and (111) surface structures. *Appl. Surf. Sci.* **2020**, *509*, 145312.

(31) Cavallotti, R.; Goniakowski, J.; Lazzari, R.; Jupille, J.; Koltsov, A.; Loison, D. Role of surface hydroxyl groups on zinc adsorption characteristics on $\alpha-Al_2O_3(0001)$ surfaces: first-principles study. *J. Phys. Chem. C* **2014**, *118*, 13578–13589.

(32) Cavallotti, R.; Thi Le, H.-L.; Goniakowski, J.; Lazzari, R.; Jupille, J.; Koltsov, A.; Loison, D. New routes for engineering the adhesion at $Zn/\alpha-Al_2O_3(0001)$ interface. *Phys. Chem. Chem. Phys.* **2016**, *18*, 3032–3039.

(33) Thi Le, H.-L.; Lazzari, R.; Goniakowski, J.; Cavallotti, R.; Chenot, S.; Noguera, C.; Jupille, J.; Koltsov, A.; Mataigne, J.-M. Tuning adhesion at metal/oxide interfaces by surface hydroxylation. *J. Phys. Chem. C* **2017**, *121*, 11464–11471.

(34) Le, H.-L. T.; Goniakowski, J.; Noguera, C.; Koltsov, A.; Mataigne, J.-M. Improving adhesion at the alumina/zinc interface by stainless steel buffers. *J. Phys. Chem. C* **2017**, *121*, 25143–25151.

(35) Messaykeh, M.; Chenot, S.; David, P.; Cabailh, G.; Jupille, J.; Koltsov, A.; Lazzari, R. An in situ and real-time plasmonic approach of seed/adhesion layers: chromium buffer effect at the

zinc/alumina Interface. *Crystal Growth & Design* **2021**, *21*, 3528–3539.

(36) Wen, C. D.; Chai, T. Y. Experimental investigation of emissivity of aluminum alloys and application of multispectral radiation thermometry. *Appl. Therm. Eng.* **2011**, *31*, 2414–2421.

(37) Konoplev, B. G.; Ageev, O. A.; Smirnov, V. A.; Kolomiitsev, A. S.; Serbu, N. I. Probe modification for scanning-probe microscopy by the focused ion beam method. *Russ. Microlectron.* **2012**, *41*, 41–50.

(38) Horcas, I.; Fernández, R.; Gómez-Rodríguez, J. M.; Colchero, J.; Gómez-Herrero, J.; Baro, A. M. WSXM: A software for scanning probe microscopy and a tool for nanotechnology. *Review of Scientific Instruments* **2007**, *78*, 013705.

(39) Doniach, S.; Sunjic, M. Many-electron singularity in X-ray photoemission and X-ray line spectra from metals. *Journal of Physics Part C : Solid State Physics* **1970**, *3*, 285–291.

(40) Shirley, D. High-resolution X-ray photoemission spectrum of valence bands of gold. *Phys. Rev. B* **1972**, *5*, 4709–4714.

(41) Kulawik, M.; Nilius, N.; Rust, H.-P.; Freund, H.-J. Atomic structure of antiphase domain boundaries of a thin Al_2O_3 film on NiAl (110). *Phys. Rev. Lett.* **2003**, *91*, 256101.

(42) McCarty, K.; Pierce, J.; Carter, C. Translation-related domain boundaries form to relieve strain in a thin alumina film on NiAl (110). *Appl. Phys. Lett.* **2006**, *88*, 141902.

(43) Schmid, M.; Shishkin, M.; Kresse, G.; Napetschnig, E.; Varga, P.; Kulawik, M.; Nilius, N.; Rust, H.-P.; Freund, H.-J. Oxygen-deficient line defects in an ultrathin aluminum oxide film. *Phys. Rev. Lett.* **2006**, *97*, 046101.

(44) Simon, G.; König, T.; Rust, H.-P.; Heyde, M.; Freund, H.-J. Atomic structure of the ultrathin alumina on NiAl (110) and its antiphase domain boundaries as seen by frequency modulation dynamic force microscopy. *New J. Phys.* **2009**, *11*, 093009.

(45) Heinke, L.; Lichtenstein, L.; Simon, G.; König, T.; Heyde, M.; Freund, H.-J. Structure and electronic properties of step edges in the aluminum oxide film on NiAl (110). *Phys. Rev. B* **2010**, *82*, 075430.

(46) Simon, G.; König, T.; Heinke, L.; Lichtenstein, L.; Heyde, M.; Freund, H.-J. Atomic structure of surface defects in alumina studied by dynamic force microscopy: strain-relief-, translation-and reflection-related boundaries, including their junctions. *New J. Phys.* **2011**, *13*, 123028.

(47) Hansen, K.; Worren, T.; Stempel, S.; Lægsgaard, E.; Bäumer, M.; Freund, H.-J.; Besenbacher, F.; Stensgaard, I. Palladium nanocrystals on Al_2O_3: structure and adhesion energy. *Phys. Rev. Lett.* **1999**, *83*, 4120.

(48) Gleason, N.; Strongin, D. A photoelectron spectroscopy and thermal desorption study of CO on FeAl (110) and polycrystalline TiAl and NiAl. *Surf. Sci.* **1993**, *295*, 306–318.

(49) Predel, B. *Ac-Ag ... Au-Zr: Supplement to Subvolume IV/5A*; Landolt-Börnstein-Group IV Physical Chemistry 12A: Physical Chemistry; Springer-Verlag Berlin Heidelberg, 2006; pp 1–2.

(50) Kubaschewski, O. *Iron binary phase diagrams*; Springer, Berlin, Heidelberg, 2013.

(51) NIST X-ray photoelectron spectroscopy database. https://srdata.nist.gov/xps/Default.aspx.

(52) Kizilkaya, O.; Hite, D.; Zehner, D.; Sprunger, P. Formation of aluminum oxide thin films on FeAl(110) studied by STM. *Surface Science* **2003**, *529*, 223–230.

(53) Kizilkaya, O.; Senevirathne, I.; Sprunger, P. The electronic structure of ultrathin aluminum oxide film grown on FeAl (110): A photoemission spectroscopy. *J. Appl. Phys.* **2007**, *101*, 063706.

Graphical TOC Entry